Accepted Manuscript

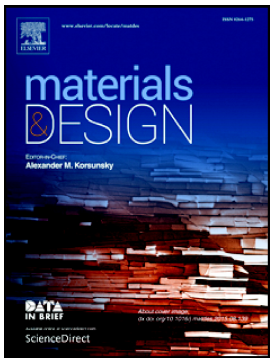

Simultaneous improvement in strength and plasticity of Ti-24Nb-4Zr-8Sn manufactured by selective laser melting

C.L. Yang, Z.J. Zhang, S.J. Li, Y.J. Liu, T.B. Sercombe, W.T. Hou, P. Zhang, Y.K. Zhu, Y.L. Hao, Z.F. Zhang, R. Yang

PII: S0264-1275(18)30566-5
DOI: doi:10.1016/j.matdes.2018.07.036
Reference: JMADE 4069

To appear in: *Materials & Design*

Received date: 6 May 2018
Revised date: 16 July 2018
Accepted date: 17 July 2018

Please cite this article as: C.L. Yang, Z.J. Zhang, S.J. Li, Y.J. Liu, T.B. Sercombe, W.T. Hou, P. Zhang, Y.K. Zhu, Y.L. Hao, Z.F. Zhang, R. Yang , Simultaneous improvement in strength and plasticity of Ti-24Nb-4Zr-8Sn manufactured by selective laser melting. Jmade (2018), doi:10.1016/j.matdes.2018.07.036

Simultaneous improvement in strength and plasticity of Ti-24Nb-4Zr-8Sn manufactured by selective laser melting

C. L. Yang [a,c], Z. J. Zhang [a], S. J. Li [a*], Y. J. Liu [b], T. B. Sercombe [b], W. T. Hou [a], P. Zhang [a], Y. K. Zhu [a], Y. L. Hao [a], Z. F. Zhang [a*] and R. Yang [a]

[a] *Institute of Metal Research, Chinese Academy of Sciences, 72 Wenhua Road, Shenyang 110016, P.R. China*

[b] *School of Mechanical and Chemical Engineering, The University of Western Australia, Crawley WA 6009, Australia*

[c] *University of Chinese Academy of Sciences, 19 Yuquan Road, Beijing 100049, P.R. China*

Abstract

The strength and plasticity of metallic materials usually exhibit a trade-off relation. This study reports a simultaneous improvement in the ultimate tensile strength (UTS) and uniform elongation (UE) of Ti-24Nb-4Zr-8Sn (Ti2448) fabricated by selective laser melting (SLM), relative to those produced via forging. Detailed microstructural characterization reveals that the outstanding tensile property may result from the bi-model structure that formes during the rapid cooling associated with SLM. Coarse grains are surrounded by fine grains within the melt pool, which causes a back stress during tension. The back stress provides additional strain-hardening capacity, which postpones the initiation of necking and then leads to the simultaneous improvement of the strength and plasticity (SISP) of the Ti2448 alloy. Furthermore, the tensile property of the SLM-fabricated sample is anisotropic which is strongly related to the irregular shape of the melt pool.

Keywords: Selective laser melting; Strength and plasticity; strain hardening; bi-model structure.

*Corresponding author, Z.F. Zhang, Tel: 0086-24-83978830, Email: zfzhang@imr.ac.cn
*Corresponding author, S.J. Li, Tel: 0086-24-83978841, Email: shjli@imr.ac.cn

1. Introduction

The mechanical properties of structural materials are strongly related to their microstructures [1-3]. Recently, several manufacturing techniques have been developed in order to produce special microstructures in the pursuit of enhanced mechanical properties. For example, severe plastic deformation (SPD) technique, such as high-pressure torsion (HPT), has been used to prepare nanocrystalline metals with very high strength [4-6]. Additionally, surface plastic deformation technique, such as surface mechanical grinding (SMG), has been used to nanocrystallize the surface of coarse-grained metals in order to obtain a better combination of strength and plasticity [7, 8]. Recently, additive manufacturing (AM) has been subjected to much attention because of the ability of AM to produce complex 3D structural components directly [9, 10]. Aside from the geometric advantages of AM, the materials prepared by AM are becoming popular within materials science community as these materials often exhibit unique microstructures and therefore can result in unusual mechanical properties [11-13].

Selective laser melting (SLM) is a widely used AM technique for metallic materials [14]. Different from traditional casting process, SLM involves line by line melting of the metal powder with a high-power laser beam. Thus, the SLM-fabricated sample consists of large number of substructures (i.e. micro melt pools) [15], while the ingot produced by conventional casting is formed after a single solidification process. As a result of this feature, the mechanical properties of various alloys fabricated by SLM have been the topic of a number of studies [16, 17]. Many of these studies have concentrated on the connection between the process parameters, resulting microstructures and the mechanical properties, including tensile/compressive and fatigue properties [18-20].

One of the most widely used alloys in SLM is Ti alloy, because of its biomedical applications such as implantology and joint replacement [63]. Ti alloy is regarded as the most appropriate implant metallic material as a result of its low Yong's modulus,

high strength and corrosion resistance [64]. Recently, large amounts of studies have been focused on the mechanical properties of AM-produced (α+β)-type Ti-6Al-4V. Whereas, it has been reported that the toxic elements Al and V might lead to allergic reaction and Alzheimer's disease [65]. In addition, the large mismatch in Young's modulus between Ti-6Al-4V implants and the bone leads to the "stress-shielding" phenomenon [66]. Therefore, there is an urgent need to find alternative Ti alloys to eliminate the drawbacks of Ti-6Al-4V. β-type Ti alloys, such as Ti-35Nb-5Ta-7Zr, Ti-29Nb-13Ta-4.6Zr and Ti-24Nb-4Zr-8Sn, are attracting increasing interest because of their low Young's modulus and non-toxicity [67]. For instance, Ti-24Nb-4Zr-8Sn (abbreviated as Ti2448) exhibits a very low Young's modulus of ~42 GPa (half that of Ti-6Al-4V alloy) and a high tensile strength of ~850 MPa [21]. The superior mechanical properties make this material an attractive alternative to Ti-6Al-4V for the next generation implants. Both solid and porous Ti2448 specimens have been produced using SLM [22, 23]. However, there have been rare report about the improvement in mechanical properties throng SLM, compared with conventional manufacturing processes.

In this study, the Ti2448 alloy fabricated by SLM exhibits a simultaneous improvement in strength and plasticity (SISP), compared with those of the forged one. The connection between the microstructure of SLM-fabricated samples and their tensile properties is explained and the mechanism for the SISP is revealed. Furthermore, because of the irregular shape of the melt pool, the tensile property of the SLM-fabricated sample is anisotropic and this anisotropy has been analysed through finite element modelling.

2. Experimental procedures

2.1 Materials fabrication.

The Ti2448 powder was produced using electrode induction melting gas atomization (EIGA) and was sieved to be 45 - 106 μm in size, with an average size

(d_{50}) of 69 μm. Parts were produced using a Realizer SLM100 with an alternating scanning strategy (that is the scanning vectors were rotated 90° between layers and the stripe size is 3 mm, as shown in Fig. 1), a scan speed of 1000 mm/s, laser power of 200 W, a hatch spacing (distance between two scan lines) of 0.1 mm and a layer thickness of 0.05 mm. A high purity (<1000 ppm O_2) argon atmosphere was used to minimise oxidation and parts were built on a titanium substrate, heated to 200 °C. Cylinders with 7 mm diameter and 60 mm long were built at four orientations. As shown in Fig. 1, the nomenclature for the orientations were: [001] direction – the Z-axis (i.e. building direction); [100] direction – the X-axis of the machine (i.e. parallel to the front of the machine and perpendicular to Z); [010] direction – the Y-axis of the machine (i.e. perpendicular to X and Z). The samples were named after the direction of their tensile axis. For example, 001 sample is strained along [001] direction and 101 sample is strained along [101] direction. Some of the SLM samples were annealed at 750 ºC in argon for an hour and cooled with furnace. An ingot of the Ti2448 alloy with diameter of 280 mm was fabricated by vacuum arc melting, using a Ti-Sn master alloy and pure Ti, Nb and Zr as raw materials. The ingot was then hot forged at 850°C to form a round bar with a diameter of 55 mm. Rod tensile samples were then prepared along the axial direction with a nominal gauge section of 15×ϕ4 mm^3.

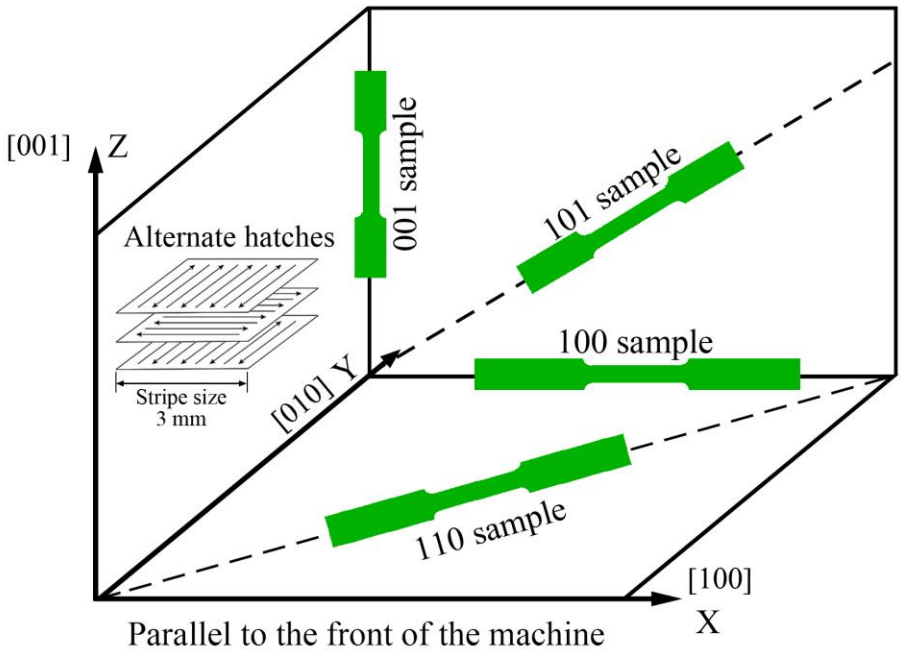

Fig. 1. The nomenclature for the orientations and the tensile specimens. The tensile specimens are named after the directions of their tensile axis.

2.2 Mechanical tests.

Tensile tests were carried out according to ISO 6892, using an INSTRON 5982 testing machine with a strain rate of 10^{-4} s^{-1} at room temperature in air. Five tests were conducted for each condition. In order to characterize the back stress, loading-unloading-reloading tensile tests were performed. The microhardness of the SLM-fabricated 100 sample was measured by a LECO AMH43 automatic hardness tester fitted with a Vickers indenter, using a load of 100 g and a hold time of 13 s. The distance between any two neighboring indentations was 50 μm.

2.3 Microstructural characterization.

The microstructure of the SLM-fabricated sample was characterized by laser scanning confocal microscopy (LSCM) and electron backscattered diffraction (EBSD). The samples for optical microscopy were mechanically polished and then etched in boiling hydrochloric acid. EBSD samples were prepared by electro-polishing at 20 °C in a 10:6:1 volume ratio of methanol, normal butanol and perchloric acid. In order to study the dislocation configuration of the SLM-fabricated sample, TEM specimens were produced by slicing the gauge section of the specimens after tensile tests (parallel to the loading direction) using wire EDM. Specimens had an original thickness of 500 μm and were then mechanically reduced to ~50 μm thick. Final polishing was performed using conventional twin-jet polishing. TEM observation was performed on an FEI Tecnai F20 transmission electron microscope with an operating voltage of ~200 kV. EBSD was used to get the crystal orientation information of a strained specimen surface, in order to determine the nature of the deformation bands on the surface of SLM-fabricated sample.

3. Experimental results

3.1 Microstructural characterizations.

The SLM-fabricated samples consist of large amounts of microscale melt pools which can be readily observed with an optical microscope, as shown in Fig. 2. The three-dimensional structure of the melt pool is irregular and thus its profile on different direction is different. Microhardness tests show that the hardness of the edge of melt pools is higher (260 ± 5 HV) than that of the center (240 ± 5 HV), as shown in Fig. 3(a). The difference between the hardness of the edge and the center of the melt pool is likely a result of the particular distribution of coarse and fine grains in the SLM-fabricated sample. This can be clearly seen in the EBSD image shown in Fig. 3(b). In this figure, it is clear that fine grains are distributed along the edge of the melt pool and the coarse grains lie at the center. The fine grains along the melt pool edge is approximate equiaxial with an grain size of ~10 μm, while the coarse grains at the melt pool center exhibit a columnar shape with the long axis parallel to the building direction. The length and width of the coarse grains are ~200 μm and ~100 μm, respectively, and thus the aspect ratio is about 2. Therefore, the SLM-fabricated sample consists of "hard-wraps-soft" structural units. This is quite different from the homogeneous microstructure of the forged sample, as shown in Fig. 3(c). In order to verify the effect of the unique microstructure on the tensile properties of the SLM-fabricated sample, an annealing heat treatment (1hr at 750°C) was also conducted on some SLM-fabricated samples to eliminate the "hard-wraps-soft" microstructure. As a result of this heat treatment the unique grain arrangement has changed to uniform coarse grains, as shown in Fig. 3(d).

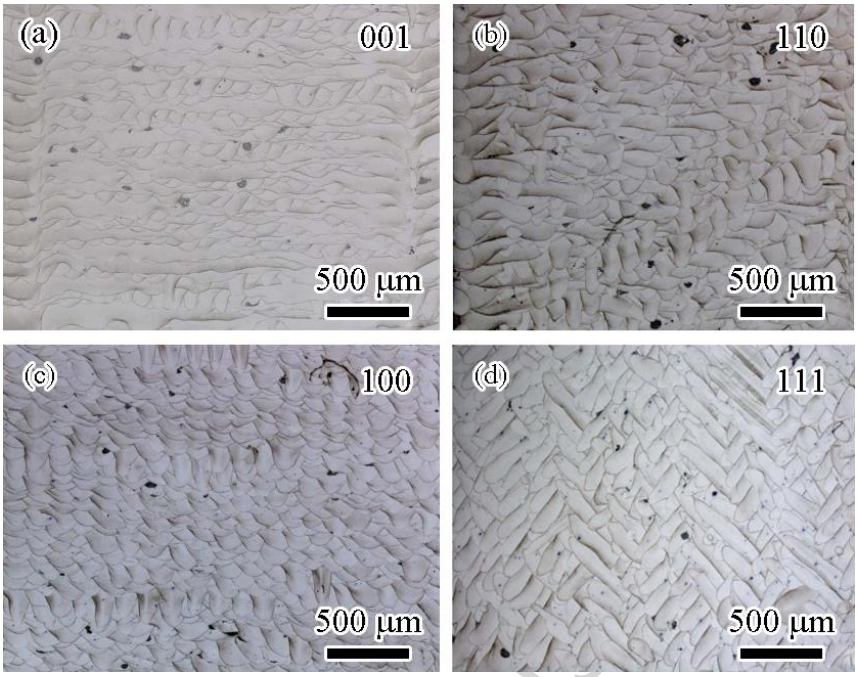

Fig. 2. The profile of melt pools in the SLM-fabricated samples. (a) [001] direction; (b) [110] direction; (c) [100] direction and (d) [111] direction.

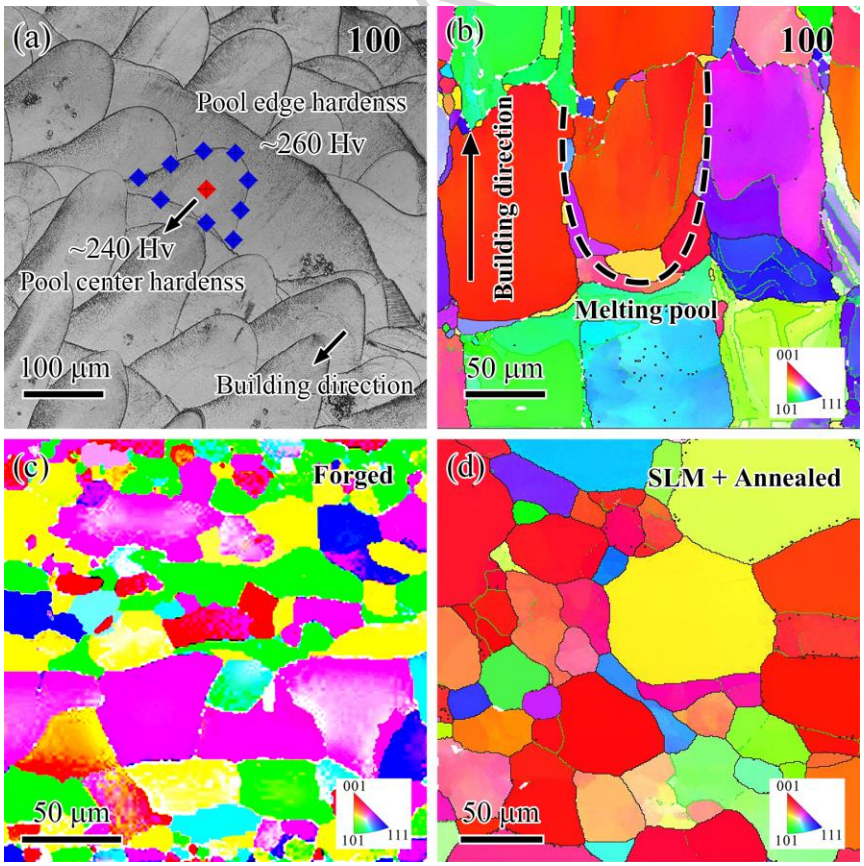

Fig. 3. Microstructure of Ti2448 before tensile tests. (a) Microscale melt pools observed by LSCM. (b) The EBSD image of the SLM-fabricated sample. The fine

grains are distributed along the edge of the melt pool and the coarse grains are at the center. (c) The EBSD image of the forged sample. (d) The EBSD image of the annealed SLM-fabricated sample.

3.2 Tensile properties.

Fig. 4 compares the results of the tensile tests conducted on the SLM-fabricated samples with those conducted on the forged and annealed material. The nomenclature for the specimen is described in Fig. 1. It is apparent that, relative to the forged and annealed samples, the SLM-fabricated samples exhibit higher ultimate tensile strength (UTS) and larger uniform elongation (UE). It is also clear that the tensile properties of the SLM-fabricated samples vary with direction, as shown in Fig. 4(a). The UTS, UE and yield strength (YS) of the 100, 110 and 101 samples are similar, whereas, those of the 001 sample are lower, which has been reported in other materials produced using SLM [24]. Besides, the as-built SLM samples exhibit an upper yield point, followed by a decrease in flow stress as strain increases. This yielding behavior is not presented in either the forged material or the annealed SLM parts. In Fig. 4(b), the σ_b/E (ultimate tensile strength and Young's modulus ratio) and UE of several Ti-based alloys fabricated through different manufacturing processes are summarized. It can be seen that the SLM-fabricated Ti2448 exhibit a better combination of strength and plasticity compared with other alloys or other manufacturing methods.

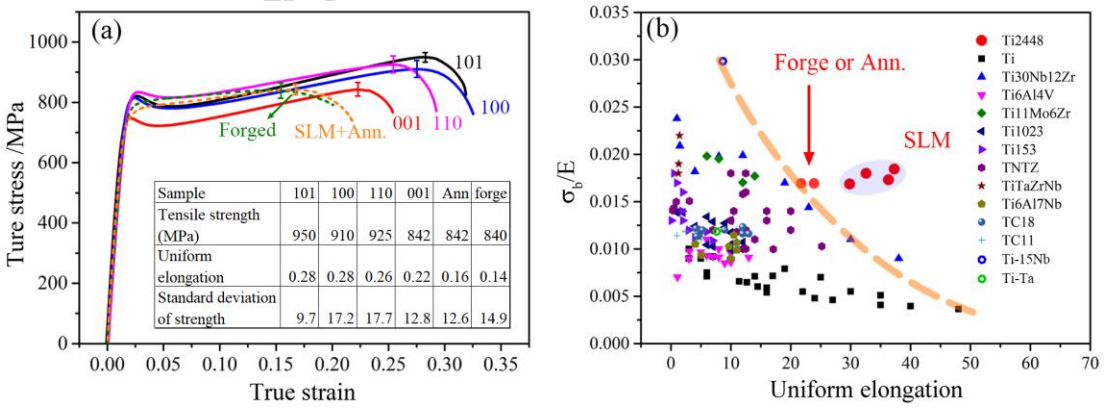

Fig. 4. The results of the tensile tests. (a) The true stress-true strain curves of the SLM-fabricated and the forged samples. The UTS and UE of the as-built SLM samples are higher than those of the annealed SLM or forged material. (b) The

σ_b/E-UE plot (with the UE calculated from displacement) of Ti-based alloys manufactured by conventional processes and SLM [40-52, 68, 69].

3.3 Post-tensile testing microstructure.

During tensile testing, some deformation bands appear on the surface, as shown in Fig. 5(a). The plastic deformation mechanism of Ti-Nb alloys varies with compositions. Saito et al. [25] reported that the plastic deformation of "gum metals" occurs via "giant fault". Plancher et al. [26] found that the "giant fault" mechanism appears to be a phase-transformation-assisted twinning mechanism. On the other hand, a large number of studies [27-29] underlined the presence and activity of dislocations in Ti-Nb alloys. In order to reveal the plastic deformation mechanism of the SLM-fabricated Ti2448, EBSD analysis was carried out (overlay in Fig. 5(a)), which provides the orientation information of the surface crystals of the sample. Based on the orientation information, the direction of the slip plane of the BCC lattice on the sample surface can be determined. The angle between the direction of the {110} plane and the deformation bands is less than 5°. Thus, it seems reasonable to conclude that the deformation bands observed on the surface of the sample are caused by dislocation slip. TEM observation verifies the existence of dislocations, as shown in Fig. 5(b), which shows the microstructure of the SLM-fabricated sample strained about 10%.

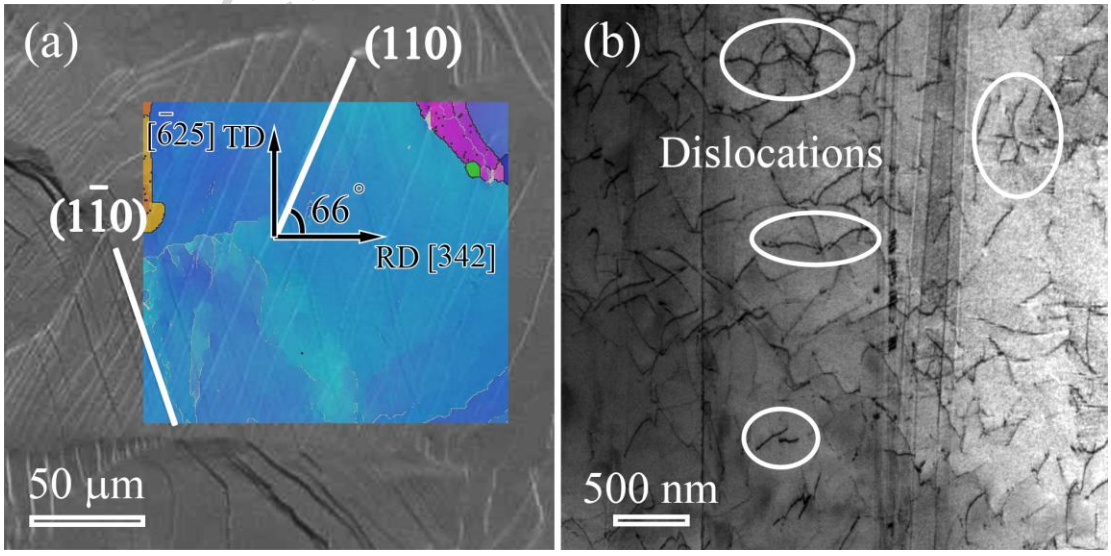

Fig. 5. Plastic deformation mechanism of the SLM-fabricated 110 samples. (a) The surface of the SLM-fabricated sample with a strain of 10% overlaid with the EBSD images showing that the deformation bands are dislocation slip planes. (b) The TEM image of the SLM-fabricated sample with a strain of 10%. Dislocations distribute randomly.

4. Discussion

Based on the experimental results above, it can be concluded that the SLM-fabricated Ti2448 shows outstanding tensile properties in two aspects: 1) higher YS; and 2) higher UTS and larger UE, accordingly displaying SISP. The mechanisms of the outstanding tensile property are discussed below.

4.1 The origin of higher yield strength.

The higher YS of the SLM-fabricated Ti2448 can be related to the "hard-wraps-soft" structure of the microscale melt pools. Based on the model of double piling-up of dislocations, the number of piled-up dislocations (n) in one array with a piling-up space L under a shear stress τ can be written as [30]:

$$n = \frac{\pi\tau L(1-\nu)}{\mu b}, \tag{1}$$

in which ν is the Poisson's ratio, μ is shear modulus and b is the Burgers vector. At the very beginning of plastic deformation, dislocations rarely entangle with each other and can glide freely for large distances. On the basis of an average assumption, the piling-up space L can be the half of the grain diameter, $0.5d$. Based on Orowan estimation of the strain relaxation after the sweeping over of a dislocation [31], the spacing between dislocations can be expressed as:

$$h = \frac{\mu b}{2\tau}. \tag{2}$$

Thus, the expression hL represents the average area occupied by one array of piled-up dislocations. In terms of yielding theory of polycrystals, when yield occurs,

dislocations pile up at grain boundaries with a concentration stress $\tau_c = n\tau$ [30], whose value should be approximately constant for all microstructures, irrespective of their grain size. Therefore, the effect of grain size on the dislocation density ρ at the yield point can be estimated as:

$$\rho = \frac{n}{hL} = \frac{\tau_c / \tau}{hL} = \frac{4\tau_c}{\mu b} d^{-1}. \quad (3)$$

A similar reciprocal relationship between grain size and dislocation density was also obtained in a recent theoretical study of Ni alloys [32]. By combining this with the Taylor equation ($\tau = \alpha\mu b\sqrt{\rho}$), the Hall-Petch relation can be derived. According to Eq. (3), with the decrease of grain size, the density of dislocations required for yielding increases. Therefore, at yield point, the flow stress of fine grains should be higher than that of coarse grains. For the SLM-fabricated samples, although some coarse grains exist, they are surrounded by fine ones, as shown in Fig. 3(b). In this case, only when the applied stress is high enough to trigger large amounts of dislocations in the fine grains that the whole specimen can deform uniformly. Therefore, the YS of the SLM-fabricated sample may be mainly controlled by the fine grains, which should be the origin of the higher YS. This strengthening mechanism is consistent with the previous observations [11, 12]. The higher YS is followed by a decrease in stress as strain increases, which can also be explained by the "hard-wraps-soft" structure of the microscale melt pools. Once the applied stress is high enough to trigger dislocations in the fine grains, the whole specimen yields. After that, plastic deformation will be mainly undertaken by the soft region (i.e. the coarse grains) and therefore the required flow stress decreases. This is quite different from the dislocation-starvation mechanism which has previously been proposed in other alloys [33, 34]. The reason for this is that the dislocation-starvation mechanism would not explain the disappearance of the upper yield point upon annealing, as annealing would result in a lower dislocation density than in the as-built condition.

4.2 The higher strength and larger plasticity.

According to the Considère criterion [35], necking initiates when the value of true stress equals to that of strain-hardening rate ($\Theta=\frac{\partial\sigma}{\partial\varepsilon}$) during tension. At this point, the UTS and the UE are reached. Thus, if the strain-hardening capability of the tensile sample can be improved, necking will be postponed and the UTS and UE will both be improved. An increase in the strain-hardening capability of the as built Ti2448 may be a result of the "hard-wraps-soft" structure of the melt pool and will be discussed as below.

The "hard-wraps-soft" structure provides additional strain-hardening capability. During tensile tests, the soft coarse grains start plastically deforming first. However, as they are constrained by the surrounding hard fine grains, causing dislocations to pile up at grain boundaries in the coarse grains [36], which is known to produce a long-range back stress [37-39]. As discussed above, the flow stress of the fine grains is higher than that of the coarse ones, and thus the plastic strain will largely occur within the softer coarse-grain region. In contrast, it is expected that the fine grains will not deform significantly. As such, a plasticity mismatch will appear at the interface between the coarse and fine grains, which needs to be accommodated by geometrically necessary dislocations (GNDs). The existence of these dislocations is determined by the shape of the plasticity mismatch region and thus, unlike the statistical storage dislocations (SSDs), they cannot be easily annihilated. Thus, these GNDs will be largely conserved during plastic deformation. In contrast specimens with uniform grains would not contain such plasticity mismatch and therefore the GNDs are not needed. Therefore relative to a uniform structure, the accumulation of the GNDs in the "hard-wraps-soft" structure will lead to an additional improvement in the flow stress and thus in the strain hardening.

To verify the existence of the back stress, cyclic loading-unloading tests were conducted on both the SLM-fabricated and forged Ti2448 and the results are shown in Fig. 6(a). It is clear that, relative to the forged material, the SLM-fabricated sample shows a stronger Bauschinger effect; that is, the unloading curve does not overlap the

reloading one and a large hysteresis loop is observed. In addition, the hysteresis loop for the SLM-fabricated sample becomes larger as the strain increases. From the shape of the hysteresis loop, a value of the back stress at the unloading point can be calculated as shown in Fig. 6(b). Using this approach, the back stress of the SLM-fabricated sample was calculated to be ~545 MPa at a strain of ~6.5% and ~558 MPa at a strain of ~9.5%, while the back stress of the forged sample is around 375 MPa and its increase with strain is negligible considering the calculation err. Also shown in Fig. 6(a) is the fact that the flow stresses of the forged and the SLM-fabricated samples were nearly the same at the first unloading point (at a strain of ~6.5%), while at 9.5% strain, the flow stress of the SLM-fabricated sample was about 10 MPa higher than that of the forged sample. This improvement in the flow stress can be attributed to the increase of the back stress. The fact that the back stress increases with increasing strain may also be explained by the accumulation of the GNDs between coarse and fine grains. During plastic deformation, the flow stress in the fine grains is higher than that in coarse grains, because of the difference in their flow stresses at yielding. As such, plastic deformation would still be undertaken by the soft coarse grains, and mismatch dislocations are still needed to account for the plasticity mismatch. Thus, as long as the difference of the flow stress exists between coarse and fine grains, GNDs will be increasingly as the strain increases. Therefore, the back stress in the "hard-wraps-soft" structure is expected to increase with the strain. The flow stress in the "hard-wraps-soft" structure can be written as:

$$\sigma = \sigma_{grain} + \sigma_{dis} + \sigma_{back}, \quad (4)$$

where σ_{grain}, σ_{dis} and σ_{back} are the stresses contributed by grain boundaries, dislocation densities and back stress, respectively. The sum of σ_{grain} and σ_{dis} can be regarded as the flow stress in uniform structures. As mentioned above, the additional back stress in the "hard-wraps-soft" structure increases as increasing strain. Therefore, the "hard-wraps-soft" structure exhibits additional strain hardening relative to the uniform structures, which serves to postpone the initiation of necking and improve the UTS and UE of the SLM-fabricated samples.

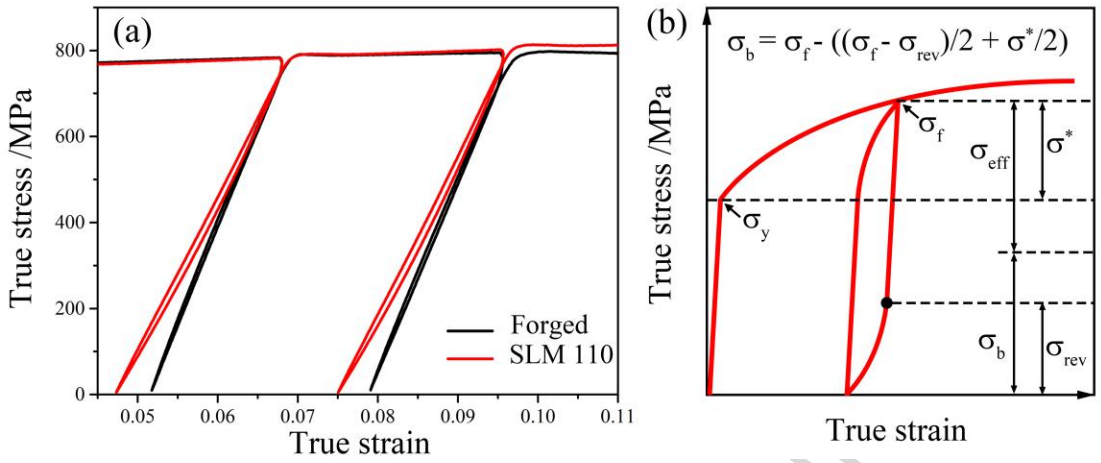

Fig. 6. (a) The loading-unloading-reloading curves of the forged and SLM-fabricated samples, which suggests an increasing back stress of the SLM-fabricated sample relative to the forged one. (b) The schematic illustration of the calculation method of back stress.

In order to exhibit the improvement of the strain-hardening capability, the strain-hardening rate curves of the both SLM-fabricated and forged samples are plotted in Fig. 7. It is clear that the Θ value of the SLM-fabricated sample is larger than that of the forged one and thus the necking of the SLM-fabricated samples occurs later. Therefore, the SISP observed in the SLM-fabricated Ti2448 can be attributed to the high strain-hardening capability caused by the "hard-wraps-soft" structure. The results reported in this work are expected to provide new directions in the microstructure design of metallic materials through AM techniques to achieve unique mechanical properties.

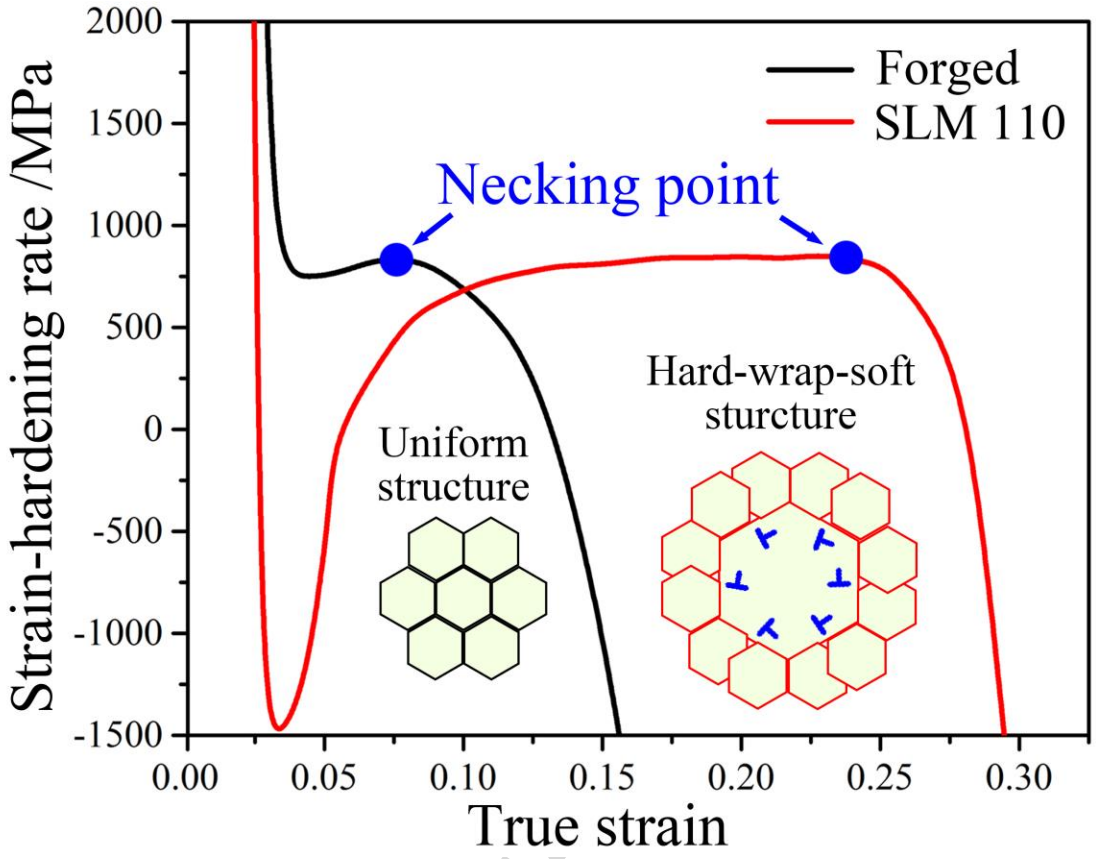

Fig. 7. The strain-hardening rate of the SLM-fabricated and forged sample. "Hard-wraps-soft" structure provides additional strain-hardening capability and then postpones the initiation of necking.

4.3 The anisotropy of the tensile property.

Previous studies attributed the anisotropy in mechanical properties of SLM-fabricated samples to the inhomogeneous microstructures. Yang et al. [60] presented a detailed study on the effect of heat treatment on the anisotropy in the mechanical properties of SLM-fabricated A357 alloy and concluded a homogenous distribution of particles and microstructures leads to a reduction in anisotropy in strength and ductility. AlMangour et al. [61] emphasized the role of texture on the anisotropy in mechanical properties of SLM-fabricated TiCp/316L stainless steel. Alsalla et al. [62] attributed the anisotropy in mechanical properties of SLM-fabricated Ti-6Al-4V to the different microstructure along different build orientation. The anisotropy in the tensile property of the SLM-fabricated Ti2448 may

also be explained by the inhomogeneous microstructure of the as-bulit sample. As mentioned above, the "hard-wraps-soft" structure provides additional strain hardening, which is caused by back stress. We propose that the back stress of the SLM-fabricated samples varies along different directions, which will be illustrated by finite element modelling (FEM) as below. For simplicity, the melt pool was modelled as two different phases: the edge with a higher YS and lower Θ and the center with a lower YS and higher Θ. The remaining material inside the box was given the same properties as the centre of the melt pool. As discussed above, the soft center will plasticly deform first but is constrained by the surrounding hard edge. Only when the hard edge yields can the entire specimen plastically deform. This leads to increased strain hardening in the soft centre, which reflects the back stress of the "hard-wraps-soft" structure at yielding. The dual phase melt pool model was strained along two directions, i.e. [001] and [100], until the edge had mostly yielded (see Fig. 8(a) and (b)). The average von-Mises stresses of the soft centre were then calculated for the two loading directions and the results are shown in Fig. 8(c) and (d). It is apparent that the average stress in the (soft) centre grains was approximately 15 MPa higher when the material was loaded in the [100] direction (Fig 5(d)) than along the [001] direction (Fig 5(c)). That is, the back stress along the [100] direction is higher than that along [001] direction. As discussed above, the higher back stress leads to a greater amount of strain hardening and therefore the strain-hardening capability of the "hard-wraps-soft" structure along [100] direction is higher than that along [001] direction. This leads to the higher UTS and UE of the 100 sample relative to those of the 001 one (Fig 4(a)).

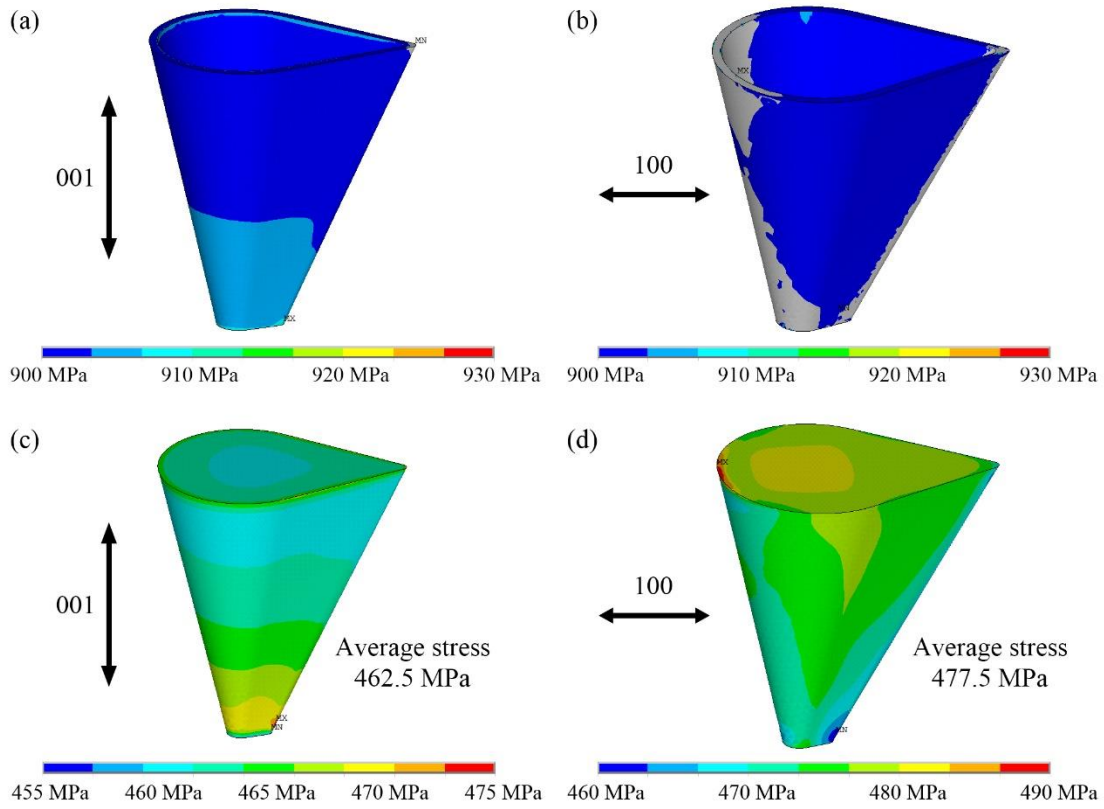

Fig. 8. The FEM results of the melt pool strain along [001] and [100] directions. (a) and (b) show the Mises stress distribution of the edge strained along [001] and [100] direction, respectively. The edge strained along [001] has fully yielded while the edge strained along [100] mostly yields. (c) and (d) show the von-Mises stresses of the center strained along [001] and [100] direction, respectively. It is obvious that the average Mises stress of the center strained along [100] is higher than that along [001] direction, which suggests a larger back stress along [100] direction for the melt pool structure.

5. Conclusions

In summary, the yield strength, ultimate tensile strength and uniform elongation of the SLM-fabricated Ti2448 are all superior to those of the conventional forged material. The simultaneous improvement of strength and plasticity has been attributed to the unique structure formed during selective laser melting, i.e. “hard-wraps-soft” structure of the microscale melt pools. The hard, fine grains distributed along the edge of the melt pool contribute to the higher yield of the SLM-fabricated Ti2448. The

"hard-wraps-soft" structure provides additional strain-hardening capability, which postpones necking and therefore improves the ultimate tensile strength and uniform elongation simultaneously.

Acknowledgements

This work was supported partially by Chinese MoST (2017YFC1104901, 2016YFC1102601), National Natural Science Foundation of China (51101162, 51201165, 51331007 and 51631007), Key Research Program of Frontier Sciences, CAS (QYZDJ-SSW-JSC031).

Author contributions

Y.L.H. designed such kind of Ti-24Nb-4Zr-8Sn alloy. T.B.S., W.T.H and Y.J.L prepared the SLM-fabricated Ti-24Nb-4Zr-8Sn alloy. C.L.Y. conducted the mechanical experiments, wrote the main manuscript and drew Figures 1-5. C.L.Y., Z.J.Z., S.J.L, P.Z. and Z.F.Z. proposed the models and mechanisms. Y.K.Z. conducted the finite element modelling. C.L.Y., S.J.L, and Z.F.Z. analysed the data and wrote the paper. Z.F.Z. and R.Y. revised the paper. All authors contributed to the scientific discussions.

References

1. X.H. An, S.D. Wu, Z.F. Zhang, R.B. Figueiredo, N. Gao, T.G. Langdon, Enhanced strength-ductility synergy in nanostructured Cu and Cu-Al alloys processed by high-pressure torsion and subsequent annealing. Scr. Mater. 66 (2012) 227-230.
2. Z.J. Zhang, X.H. An, P. Zhang, M.X. Yang, G. Yang, S.D. Wu, Z.F. Zhang, Effects of dislocation slip mode on high-cycle fatigue behaviors of ultrafine-grained Cu-Zn alloy processed by equal-channel angular pressing. Scr. Mater. 68 (2013) 389-392.

3. A. Khalajhedayati, Z. Pan, T.J. Rupert, Manipulating the interfacial structure of nanomaterials to achieve a unique combination of strength and ductility. Nat. Commun. 7 (2016) 10802.
4. Y.Z. Tian, L.J. Zhao, N. Park, R. Liu, P. Zhang, Z.J. Zhang, A. Shibata, Z.F. Zhang, N. Tsuji, Revealing the deformation mechanisms of Cu-Al alloys with high strength and good ductility. Acta Mater. 110 (2016) 61-72.
5. X. Liu, Y. Liu, B. Jin, Y. Lu, J. Lu, Microstructure Evolution and Mechanical Properties of a SMATed Mg Alloy under In Situ SEM Tensile Testing. J. Mater. Sci. Tech. 33 (2017) 224-230.
6. P.V. Liddicoat, X.Z. Liao, Y.H. Zhao, Y.T. Zhu, M.Y. Murashkin, E.J. Lavernia, R.Z. Valiev, S.P. Ringer, Nanostructural hierarchy increases the strength of aluminium alloys. Nat. Commun. 1 (2010) 63.
7. K. Lu, Making strong nanomaterials ductile with gradients. Science 345 (2014) 1455-1456.
8. Q. Qin, S.Yin, G.M. Cheng, X.Y. Li, T.H. Chang, G. Richter, Y. Zhu, H.J. Gao, Recoverable plasticity in penta-twinned metallic nanowires governed by dislocation nucleation and retraction. Nat. Commun. 6 (2015) 5983.
9. C.Y. Yap, C.K. Chua, Z.L. Dong, Z.H. Liu, D.Q. Zhang, L.E. Loh, S.L. Sing, Review of selective laser melting: Materials and applications. Appl. Phys. Rev. 2 (2015) 041101.
10. K.G. Prashanth, S. Scudino, A.K. Chaubey, L. Lober, P. Wang, H. Attar, F.P. Schinansky, F. Pyczak, J. Eckert, Processing of Al–12Si–TNM composites by selective laser melting and evaluation of compressive and wear properties. *J.* Mater. Res. 31 (2015) 55-65.
11. S. Scudino, C. Unterdorfer, K.G. Prashanth, H. Attar, N. Ellendt, V. Uhlenwinkel, J. Eckert, Additive manufacturing of Cu–10Sn bronze. Mater. Lett. 156 (2015) 202-204.
12. W. Xu, M. Brandt, S. Sun, J. Elambasseril. Q. Liu, K. Latham, K. Xia, M. Qian, Additive manufacturing of strong and ductile Ti–6Al–4V by selective laser melting via in situ martensite decomposition. Acta Mater. 85 (2015) 74-84.
13. H. Zhang, H. Zhu, T. Qi, Z. Hu, X. Zeng, Selective laser melting of high strength Al–Cu–Mg alloys: Processing, microstructure and mechanical properties. Mater. Sci. Eng. A 656 (2016) 47-54.
14. L.C. Zhang, H. Attar, M. Calin, J. Eckert, Review on manufacture by selective laser melting and properties of titanium based materials for biomedical applications. Mater. Tech. 31 (2016) 66-76.
15. K.G. Prashanth, J. Eckert, Formation of metastable cellular microstructures in selective laser melted alloys, J. Alloy. Comp. 707 (2017) 27-34.
16. Y.J. Liu, S.J. Li, H.L. Wang, W.T. Hou, Y.L. Hao, R. Yang, T.B. Sercombe, L.C. Zhang, Microstructure, defects and mechanical behavior of beta-type titanium porous structures manufactured by electron beam melting and selective laser melting. Acta Mater. 113 (2016) 56-67.
17. V. Cain, L. Thijs, J. Van Humbeeck, B. Van Hooreweder, R. Knutsen, Crack

propagation and fracture toughness of Ti6Al4V alloy produced by selective laser melting. Addit. Manuf. 5 (2015) 68-76.

18. K.G. Prashanth, S. Scudino, J. Eckert, Defining the tensile properties of Al-12Si parts produced by selective laser melting, Acta Mater. 126 (2017) 25-35.
19. Z. Wang, R.T. Qu, S. Scudina, B.A. Sun, K.G. Prashanth, D.V. Louzguine-Luzgin, M.W. Chen, Z.F. Zhang, J. Eckert, Hybrid nanostructured aluminum alloy with super-high strength, NPG Asia Mater. 7 (2015) e229.
20. X.P. Li, X.J. Wang, M. Saunders, A. Suvorova, L.C. Zhang, Y.J. Liu, M.H. Fang, Z.H. Huang, T.B. Sercombe, A selective laser melting and solution heat treatment refined Al-12Si alloy with a controllable ultrafine eutectic microstructure and 25% tensile ductility. Acta Mater. 95 (2015) 74-82.
21. Y.L. Hao, S.J. Li, S.Y. Sun, C.Y. Zheng, R. Yang, Elastic deformation behaviour of Ti–24Nb–4Zr–7.9Sn for biomedical applications. Acta Biomater. 3 (2007) 277-286.
22. L.C. Zhang, D. Klemm, J. Eckert, Y.L. Hao, T.B. Sercombe, Manufacture by selective laser melting and mechanical behavior of a biomedical Ti-24Nb-4Zr-8Sn alloy. Scr. Mater. 65 (2011) 21-24.
23. Y.J. Li, X.P. Li, L.C. Zhang, T.B. Sercombe, Processing and properties of topologically optimised biomedical Ti-24Nb-4Zr-8Sn scaffolds manufactured by selective laser melting. Mater. Sci. Eng. A 642 (2015) 268-278.
24. I. Tolosa, F. Garciandía, F. Zubiri, F. Zapirain, A. Esnaola, Study of mechanical properties of AISI 316 stainless steel processed by "selective laser melting", following different manufacturing strategies. Int. J. Adv. Manuf. Technol. 51 (2010) 639-647.
25. T. Saito, T. Furuta, J.H. Hwang, S. Kuramoto, K. Nishino, N. Suzuki, R. Chen, A. Yamada, K. Ito, Y. Seno, T. Nonaka, H. Ikenhata, N. Nagasako, C. Iwamoto, Y. Ikuhara, T. Sakuma, Multifunctional alloys obtained via a dislocation-free plastic deformation mechanism. Science 300 (2003) 464-467.
26. E. Plancher, C.C. Tasan, S. Sandloebes, D. Raabe, On dislocation involvement in Ti-Nb gum metal plasticity. Scr. Mater. 68 (2013) 805-808.
27. W.Y. Guo, H. Xing, J. Sun, X.L. Li, J.S. Wu, R. Chen, Evolution of microstructure and texture during recrystallization of the cold-swaged Ti-Nb-Ta-Zr-O alloy. Metall. Mater. Trans. A 39A (2008) 672-678.
28. H. Xing, J. Sun, Q. Yao, W.Y. Guo, R. Chen, Origin of substantial plastic deformation in Gum Metals. *Appl. Phys. Lett*. **92** (2008) 151905.
29. Y. Yang, S.Q. Wu, G.P. Li, Y.L. Li, Y.F. Lu, K, Yang, P. Ge, Evolution of deformation mechanisms of Ti-22.4Nb-0.73Ta-2Zr-1.34O alloy during straining. Acta Mater. 58 (2010) 2778-2787.
30. W.D. Callister, Fundamentals of materials science and engineering. John Wiley & Sons, Inc., USA, 2001.
31. E. Orowan, , Origin and spacing of slip bands, Nature, 147 (1941) 452-453.
32. J.A. El-Awady, Unravelling the physics of size-dependent dislocation-mediated plasticity. Nature Comm. 6 (2015) 5926.

33. X.X. Huang, N. Hansen, N. Tsuji, Hardening by annealing and softening by deformation in nanostructured metals. Science 312 (2006) 249-251.
34. M.D. Uchic, D.M. Dimiduk, J.N. Florando, W.D. Nix, Sample dimensions influence strength and crystal plasticity. Science 305 (2004) 986-989.
35. E. Plancher, C.C. Tasan, S, Sandloebes, D. Raabe, On dislocation involvement in Ti–Nb gum metal plasticity, Scr. Mater. 68 (2013) 805-808.
36. X. Wu, M.X. Yang, F.P. Yuan, G.L. Wu, Y.J. Wei, X.X. Huang, Y.T. Zhu, Heterogeneous lamella structure unites ultrafine-grain strength with coarse-grain ductility. Proc. Natl. Acad. Sci. U.S.A. 112 (2015) 14501-14505.
37. J.C. Gibeling, W.D. Nix, A numerical study of long-range internal-stresses associated with subgrain boundaries. Acta Metall. 28 (1980) 1743-1752.
38. H. Mughrabi, Dislocation wall and cell structures and long-range internal stresses in deformed metal crystals. Acta Metall. 31 (1983) 1367-1379.
39. C.W. Sinclair, G. Saada, J.D. Embury, Role of internal stresses in co-deformed two-phase materials. Philos. Mag. 86 (2006) 4081-4098.
40. C. Qin, Z. Yao, Y. Li, Y. N, H. Guo, Effect of hot working on microstructure and mechanical properties of TC11/Ti_2AlNb dual-alloy joint welded by electron beam welding process. Trans. Nonferrous Met. Soc. China 24 (2014) 3500-3508.
41. Z. Xu, Y. Zhang, M. Liu, X. Gong, Interface microstructure evolution and bonding strength of TC11/γ-TiAl bi-materials fabricated by laser powder deposition. Rare Met. 35 (2016) 456-462.
42. S. Sun, L. Wang, J. Qin, Y. Chen, W. Lu, D. Zhang, Microstructural characteristics and mechanical properties of in situ synthesized (TiB+TiC)/TC18 composites. Mater. Sci. Eng. A 530 (2011) 602-606.
43. S. Sun, W. Lv, Microstructure and mechanical properties of TC18 Titanium alloy. Rare Met. Mater. Eng. 45 (2016) 1138-1141.
44. A. Derakhshandeh, M. Nili-Ahmadabadi, A. Khajezade, H. Shahmir, Room Temperature Flow Behavior of Ti Deformed by Equal-Channel Angular Pressing Using Core–Sheath Method. Adv. Eng. Mater. 19 (2017) 1600552.
45. H. Shahmir, T.G. Langdon, Characteristics of the allotropic phase transformation in titanium processed by high-pressure torsion using different rotation speeds. Mater. Sci. Eng. A 667 (2016) 293-299.
46. M. Kimura, T. Iijima, M. Kusaka, K. Kaizu, A. Fuji, Joining phenomena and tensile strength of friction welded joint between Ti–6Al–4V titanium alloy and low carbon steel. J. Manuf. Process. 24 (2016) 203-211.
47. P. Kumar, K.S.R. Chandran, Strength–Ductility Property Maps of Powder Metallurgy (PM) Ti-6Al-4V Alloy: A Critical Review of Processing-Structure-Property Relationships. Metall. Mater. Trans. A 48 (2017) 2301-2319.
48. F.Q. Hou, S.J. Li, Y.L. Hao, R. Yang, Nonlinear elastic deformation behaviour of Ti–30Nb–12Zr alloys. Scr. Mater. 63 (2010) 54-57.
49. M. Ikeda, S. Komatsu, T. Sugimoto, M. Hasegawa, Effect of two phase warm rolling on aging behavior and mechanical properties of Ti–15Mo–5Zr–3Al

alloy. Mater. Sci. Eng. A 243 (1998) 140-145.
50. M. Okada, Strengthening of Ti-1 5V-3 C r-3Sn-3A l by Thermo-mechanical Treatments. ISIJ Inter. 31 (1991) 834-839.
51. J. Ma, Q. Wang, Aging characterization and application of Ti–15–3 alloy. Mater. Sci. Eng. A 243 (1998) 150-154.
52. Suresh Neelakantan, E.I. Galindo-Nava, D.S. Martin, J. Chao, P.E.J. Rivera-Díaz-del-Castillo. Modelling and design of stress–induced martensite formation in metastable β Ti alloys. Mater. Sci. Eng. A 590 (2014) 140-146.
53. D. Li, S. Hui, W. Ye, C. Li, Microstructure and mechanical properties of a new high-strength and high-toughness titanium alloy. Rare Met. (2016) 1-7.
54. S. Ozan, J. Lin, Y. Li, C. Wen, New Ti-Ta-Zr-Nb alloys with ultrahigh strength for potential orthopedic implant applications. J. Mech. Behav. Biomed. Mater. 75 (2017) 119-127.
55. Z. Li, B. Zheng, Y. Wang, T. Topping, Y. Zhou, R.Z. Valiev, A.Shan, E.J. Lavernia, Ultrafine-grained Ti–Nb–Ta–Zr alloy produced by ECAP at room temperature. J. Mater. Sci. 49 (2014) 6656-6666.
56. I. Kopova, J. Stráský, P. Harcuba, M. Landa, M. Janeček, L. Bačákova, Newly developed Ti–Nb–Zr–Ta–Si–Fe biomedical beta titanium alloys with increased strength and enhanced biocompatibility. Mater. Sci. Eng. C 60 (2016) 230-238.
57. J. Stráský, P. Harcuba, K. Václavová, K. Horváth, M. Landa, O. Srba, M. Janeček, Increasing strength of a biomedical Ti-Nb-Ta-Zr alloy by alloying with Fe, Si and O. J. Mech. Behav. Biomed. Mater. 71 (2017) 239-336.
58. S. Nag, R. Banerjee, Laser deposition and deformation behavior of Ti–Nb–Zr–Ta alloys for orthopedic implants. J. Mech. Behav. Biomed. Mater. 16 (2012) 21-28.
59. M. Niinoi, Mechanical properties of biomedical titanium alloys. Mater. Sci. Eng. A 243 (1998) 231-236
60. K.V. Yang, P. Rometsch, C.H.J. Davies, A. Huang., X. Wu, Effect of heat treatment on the microstructure and anisotropy in mechanical properties of A357 alloy produced by selective laser melting, Mater. Des. 154 (2018) 275-290.
61. B. AlMangour, D. Grzesiak., J. Yang, Scanning strategies for texture and anisotropy tailoring during selective laser melting of TiC/316L stainless steel nanocomposites, J. Alloy. Comp. 728 (208) 424-435.
62. H.H. Alsalla, C. Smith, L. Hao, The effect of different build orientations on the consolidation, tensile and fracture toughness properties of direct metal laser sintering Ti-6Al-4V, Rapid Prototyping J. 24 (2018) 276-284.
63. M. Geetha, A. Singh, R. Asokamani, A. Gogia, Ti based biomaterials, the ulti-mate choice for orthopaedic implantsea review, Prog. Mater Sci. 54 (2009) 397-425.
64. M. Long, H.J. Rack, Titanium alloys in total joint replacementda materials science perspective, Biomaterials 19 (1998) 1621-1639.
65. S.E. Haghighi, H. Lu, G. Jian, G. Cao, D. Habibi, L.C. Zhang, Effect of a α”

martensite on the microstructure and mechanical properties of beta-type Ti-Fe-Ta alloys, Mater. Des. 76 (2015) 47-54.

66. L.C. Zhang, D. Klemm, J. Eckert, Y.L. Hao, T.B. Sercombe, Manufacture by selective laser melting and mechanical behavior of a biomedical Ti-24Nb-4Zr-8Sn alloy, Scr. Mater. 65 (2011) 21-24.
67. Y.L. Hao, R. Yang, M. Niinomi, D. Kuroda, Y.L. Zhou, K. Fukunaga, A. Suzuki, Aging response of the young's modulus and mechanical properties of Ti-29Nb-13Ta-4.6Zr for biomedical applications, Metall. Mater. Trans. A 34 (2003) 1007-1012.
68. Q. Wang, C. Han, T. Choma, Q. Wei, C. Yan, B. Song, Y. Shi, Effect of Nb content on microstructure, property and in vitro apatite-forming capability of Ti-Nb alloys fabricated via selective laser melting, Mater. Des., 126 (2017) 268-277.
69. S.L. Sing, W.Y. Yeong, F.E. Wiria, Selective laser melting of titanium alloy with 50 wt% tantalum: Microstructure and mechanical properties, J. Alloy. Comp. 660 (2016) 461-470.

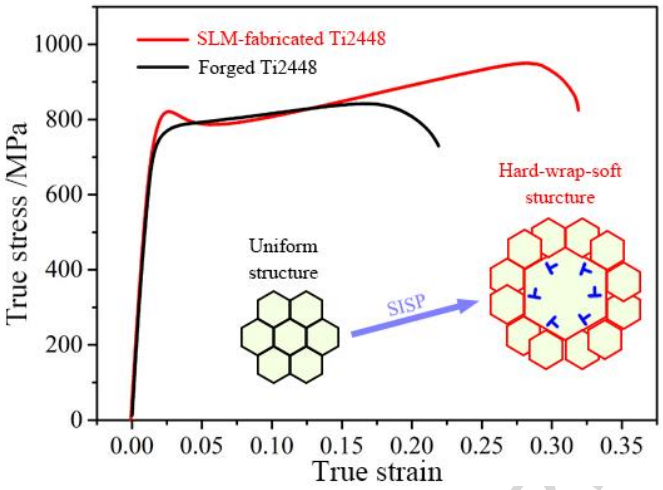

Graphical abstract

Highlights:

1. Melt pools with a bi-model structure are formed in a biocompatible Ti alloy through selective laser melting.
2. The as-built Ti alloy exhibits a better combination of strength and plasticity, relative to traditionally forged counterpart.
3. For the first time, the back stress of the melt pool along different directions are studied through finite element modeling.